



Delicate surface vacancies engineering of Ru doped MOF-derived Ni-NiO@C hollow microsphere superstructure to achieve outstanding hydrogen oxidation performance

Yuting Yang^a, Yi Huang^a, Shuqing Zhou^a, Yi Liu^a, Luyan Shi^a, Tayirjan Taylor Isimjan^{b,*}, Xiulin Yang^{a,*}

^a Guangxi Key Laboratory of Low Carbon Energy Materials, School of Chemistry and Pharmaceutical Sciences, Guangxi Normal University, Guilin 541004, Guangxi, China

^b Saudi Arabia Basic Industries Corporation (SABIC) at King Abdullah University of Science and Technology (KAUST), Thuwal 23955-6900, Saudi Arabia

ARTICLE INFO

Article history:

Received 9 April 2022

Revised 2 June 2022

Accepted 7 June 2022

Available online 14 June 2022

Keywords:

Ru/Ni-NiO@C

Vacancy defects

Electrocatalysis

Metal-organic framework

Hydrogen oxidation

ABSTRACT

Surface vacancy defects, as the bridge between theoretical structural study and the design of heterogeneous catalysts, have captured much attention. This work develops a metal-organic framework-engaged replacement-pyrolysis approach to obtain highly dispersed Ru nanoparticles immobilized on the vacancy-rich Ni-NiO@C hollow microsphere (Ru/Ni-NiO@C). Fine annealing at 400 °C introduces nickel and oxygen vacancies on Ru/Ni-NiO@C surface, resulting in an improved electrical conductivity and rapid mass-charge transfer efficiency. Ru/Ni-NiO@C with a hollow micro/nanostructure and interconnected meso-porosity favors the maximal exposure of abundant active sites and elevation of hydrogen oxidation reaction (HOR) activity. Experimental results and density functional theory (DFT) calculations reveal that an electronic effect between Ru and Ni-NiO@C, in conjunction with nickel/oxygen vacancies in the NiO species could synergistically optimize hydrogen binding energy (HBE) and hydroxide binding energy (OHBE). The HBE and OHBE optimizations thus created confer Ru/Ni-NiO@C with a mass activity over 7.75 times higher than commercial Pt/C. Our work may provide a constructive route to make a breakthrough in elevating the hydrogen electrocatalytic performance.

© 2022 Science Press and Dalian Institute of Chemical Physics, Chinese Academy of Sciences. Published by ELSEVIER B.V. and Science Press. All rights reserved.

1. Introduction

Fuel cell technologies have stimulated substantial attention by virtue of their high energy density, high energy conversion efficiency, and environmental compatibility, which lay the foundation for the sustainable development of society [1]. Among several types of fuel cells, proton exchange membrane fuel cells (PEMFCs) and hydroxide exchange membrane fuel cells (HEMFCs) are the leading hydrogen utilization techniques at low temperature [2,3]. However, the commercialization of PEMFCs is inevitably plagued by expensive Pt-based catalysts and per-fluorinated membranes. HEMFCs give critical merits over PEMFCs due to the possibility of using non-precious metal-based catalysts, milder alkaline working conditions, and cheaper bipolar plates [3]. Unfortunately, the anode hydrogen oxidation reaction (HOR) activity on precious metals is approximately two orders of magnitude drop when switching from acidic to alkali electrolytes [4,5]. There are significant differ-

ences between the HOR in alkaline ($\text{H}_2 + 2\text{OH}^- \rightarrow 2\text{H}_2\text{O} + 2e^-$) and acidic ($\text{H}_2 \rightarrow 2\text{H}^+ + 2e^-$) media [6]. Accordingly, two descriptors of hydrogen binding energy (HBE) and hydroxide binding energy (OHBE) have been reported to verify the origin of slow alkaline HOR kinetics [4,7,8]. Following Sabatier's principle, the most active HOR electrocatalysts can be correlated with the calculated HBE on the metal surfaces via a volcano relationship [9]. This correlation suggests that HBE is used as a dominant descriptor for alkaline HOR activity. However, proton donor is changed from H_3O^+ in acidic to H_2O in alkaline conditions plus the existences of OH^- species, the Volmer step is the rate-determining step in alkaline HOR [10]. Thus, a bifunctional mechanism that balanced optimal HBE and OHBE/oxophilicity has been propounded to design the alkaline HOR electrocatalysts with better performance [6,8,10]. For example, Li et al. have done pioneering works on the fabrication of BCC-phased PdCu, which showed higher HOR activity owing to the synergistic interplay between HBE and OHBE [11]. Yu et al. also demonstrated that synergistic optimization of HBE and OHBE on MoNi_4 determined the HOR activity in alkali medium [8]. Furthermore, we reported HBE and OHBE played equally important roles for the enhancement of HOR activity [12,13].

* Corresponding authors.

E-mail addresses: isimjant@sabic.com (T.T. Isimjan), xlyang@gxnu.edu.cn (X. Yang).

Ruthenium possesses the lower price and favorable Ru–H bond strength, and its HOR activity can be potentially increased to approaching that of Pt/C after fine-tuning [12,14]. Zhuang et al. showed that the HOR activity of Pt-based materials can be optimized by alloying with Ru, however, Ru shows low HOR activity. As Pt is the significant component of PtRu/C, it still has a high cost [15]. Replacing platinum metals with cheap catalysts is a critical step to tackling the inherent disadvantages of Pt-based catalysts. Ni-based materials have an emerging impact in this perspective, which are helpful for alkaline HOR, such as Ni/NiO/C [7], Ni/MoO₂ [16], and CeO₂/Ni [17], but their HOR activity and durability are still lagging far behind the benchmark Pt/C. Another plausible stratagem to enhance the HOR activity is the introduction of metal-support effect since it creates a strong metal-support interaction (SMSI), which enables to effectively steer the electronic structure and catalytic efficiency of loaded metal nanoparticles [18]. Recently, we have demonstrated that Ni₃N–Mo₂C supported Pt nanoparticles via SMSI engineering can enhance HOR activity [13]. Moreover, Speck et al. demonstrated maximizing metal and metal-oxide interfaces drastically improved HOR activity [19]. Metal-organic frameworks (MOFs) are defined as the ideal self-sacrificial templates to establish advanced transition metal/metal oxide materials. Diversified metal nodes/organic ligands and highly ordered porous architecture endow MOFs with rich coordination sites, which could help implant carbon-coated active transition metal/metal oxide species with the desired structure and induce surface defects during pyrolysis, resultantly facilitating electron transfer and promoting the electrocatalytic performance [20,21]. For instance, Thoms et al. reported porous Ni₂P prepared from a CUP-1-Ni MOF precursor [22]. The resulting Ni₂P–NPCM-900-2 was integrated as both cathode and anode to construct a two-electrode electrolyzer, which exhibited excellent performance for overall water splitting with the only need for a cell voltage of 1.62 V to generate 10 mA cm⁻². Wan et al. also reported ZnO/Ni/NiO dispersed in carbon support with a unique three-dimensional (3D) interconnected nanostructure, which exhibited excellent electrochemical properties of supercapacitors [23].

Herein, taking advantages of MOF structural tunability and tailorable compositions [7], we first synthesize Ni-MOF with defect-rich microspherical hollow structure as the starting material. We then report a replacement-pyrolysis strategy to obtain Ru/Ni-NiO@C electrocatalyst with the uniform graphene layers coating on the Ni and NiO by thermal annealing Ru doped Ni-MOF materials at 400 °C. We aim to study the micro-structures of Ru/Ni-NiO@C, and explore the possible reaction mechanism. The resultant Ru/Ni-NiO@C (sample annealed at 400 °C) manifests a potentially transformative combination of enhanced activity and high durability. Fine tuning the annealing process at 400 °C induces nickel and oxygen vacancies, which can enhance charge transfer. Density functional theory (DFT) calculations reveal that the electronic interaction between Ru and Ni-NiO@C, as well as the vacancy-rich NiO species, enable optimum adsorption of hydrogen on Ru and hydroxyl on NiO, thus boosting the key Volmer step in alkaline HOR catalysis. The attractive features of Ru/Ni-NiO@C might be promising for the rational design of HOR electrocatalyst in hydrogen fuel cells.

2. Experimental

2.1. Materials

Nickel (II) nitrate hexahydrate (Ni(NO₃)₂·6H₂O, AR, 98%, Xilong Science, 500 g), poly(vinylpyrrolidone) ((C₆H₉NO)_n, AR, 99%, PVP, Aladdin, 100 g), trimesic acid (H₃BTC, AR, 98%, Aladdin, 250 g), ruthenium trichloride (RuCl₃, AR, 99%, Ru: 37%–40%, Aladdin,

1 g), potassium hydroxide (KOH, AR, >90%, Macklin, 500 g), *N,N*-Dimethylformamide (DMF, AR, 99.5%, Xilong Science, 500 mL), ethanol (AR, 99.5%, Xilong Science, 500 mL), commercial Pt/C (20 wt% Pt, Sinero, 1 g), commercial Ru/C (5 wt% Ru, Macklin, 5 g), Nafion solution (5 wt%, Alfa Aesar, 100 mL), deionized water (18.25 MΩ cm⁻¹). All chemicals were analytical grade and could be used directly as received.

2.2. Synthesis of Ni-MOF hollow microspheres

The hollow Ni-MOF microspheres were synthesized through a hydrothermal method as following. 3 mmol Ni(NO₃)₂·6H₂O, 1.5 mmol H₃BTC, and 3.0 g PVP were added to the 60 mL mixture solution (distilled water: ethanol: DMF = 1:1:1 v/v/v). After stirring vigorously for 1 h, the solution was transferred to a 100 mL Teflon-lined stainless-steel autoclave and heated at 150 °C for 8 h. The light green powder was collected by centrifugation, washed several times with ethanol and DMF, and dried overnight at 60 °C.

2.3. Synthesis of Ru/Ni-NiO@C hybrid hollow microspheres

Dried Ni-MOF powder (50 mg) were immersed into 20 mL mixture solution (ethanol: DMF = 1:1 v/v) containing 7.2 mg RuCl₃ and allowed to react at room temperature for 10 h with stirring. The precursor was collected by centrifugation, washed twice with ethanol and dried at 60 °C overnight. The obtained precursor was then placed in a tube furnace, and heated up to 400 °C for 4 h with a heating rate of 5 °C min⁻¹ in N₂ atmosphere. After natural cooling, the as-synthesized catalyst was denoted as Ru/Ni-NiO@C, and the expected Ru content is 3.8 wt% confirmed by inductively coupled plasma (ICP) measurements. A set of Ru/Ni-NiO@C catalysts with various relative Ru loading were also prepared by varying the amount of RuCl₃ (e.g., 5.5 and 10 mg). For comparison, Ru_{2.9}/Ni-NiO@C and Ru_{5.1}/Ni-NiO@C were also synthesized by the same procedure as that of Ru/Ni-NiO@C. Similarly, Ru/NiO@C (300 °C), Ru/Ni-NiO@C-500, and Ru/Ni-NiO@C-600 were synthesized with the same method except for the pyrolysis temperatures (300, 500, and 600 °C, respectively).

2.4. Materials characterization

X-ray diffraction (XRD) patterns were measured using a Rigaku D/Max with Cu K_α (λ = 1.540598 Å) radiation. Scanning electron microscope (SEM) measurements were operated on FEI Quanta 200 system. Transmission electron microscopy (TEM) images were recorded on a JEM-2100F electron microscope equipped with an energy dispersive X-ray detector (EDX) at an acceleration voltage of 200 kV. X-ray photoelectron spectroscopy (XPS) was conducted on Kratos XSAM 800 spectrophotometer. Thermal gravimetric analysis (TGA) was carried out on a TA Instruments. The Nitrogen adsorption-desorption measurements were performed by Quantachrome AUTOSORB-IQ instrument. Raman spectra were obtained from laser micro-Raman spectrometer (Renishaw in via with a visible laser, λ = 532 nm). Electron paramagnetic resonance (EPR) spectra were measured by Bruker E500 spectrometer. Inductively coupled plasma atomic emission spectroscopy (ICP-AES) was taken on Intrepid II XSP instrument.

2.5. Computational methods

Spin-polarized DFT calculations were performed using the Vienna ab initio simulation package (VASP) [24,25]. The generalized gradient approximation proposed by Perdew, Burke, and Ernzerhof (GGA-PBE) is selected for the exchange-correlation potential [26]. The pseudo-potential was described by the projector-augmented-wave (PAW) method [27]. The geometry optimization

is performed until the Hellmann-Feynman force on each atom is smaller than $0.03 \text{ eV } \text{\AA}^{-1}$. The energy criterion is set to 10^{-6} eV in iterative solution of the Kohn-Sham equation. The Kohn-Sham valence electronic wavefunction was expanded in a plane-wave basis set with a cutoff at 400 eV. Adsorption energy was calculated according to $E_{\text{adsorption}} = E_{\text{total}} - E_{\text{substrate}} - E_{\text{adsorbate}}$.

3. Results and discussion

3.1. Synthesis and structural characterization

Forming microspherical hollow structure in the precursor requires pertinent structure engineering. We bring up a MOF-engaged replacement-pyrolysis technique to achieve such goal. Fig. 1(a) schematically depicts the synthesis process of Ru/Ni-NiO@C hollow microsphere superstructure (see Experimental methods for more details). Firstly, $\text{Ni}(\text{NO}_3)_2 \cdot 6\text{H}_2\text{O}$ is used as the Ni precursor and trimesic acid is selected as the organic ligand. Polyvinylpyrrolidone (PVP) acts as a structure-directing agent to create defect-rich hollow spherical structure for the growth of MOF via a simple hydrothermal method. The Ni-MOF with accessible large interior cavities can accommodate foreign active metals well [28]. Subsequently, the Ru precursor, RuCl_3 , may be confined to the inner and outer shells of the Ni-MOF hollow microspheres through the galvanic replacement reaction, forming a Ru/Ni-MOF hybrid structure. Finally, the thus-obtained Ru/Ni-MOF composite was heated in a tube furnace at $400 \text{ }^\circ\text{C}$ for 4 h under N_2 flow to activate the metal sites. The Ru^{3+} was converted to metallic Ru nanoparticles (NPs). Ni species in the carbonized MOF were converted into Ni-NiO@C heterojunction structure. The organic ligands were carburized to form partially graphitic support. The expected Ru content is 3.8 wt% confirmed by ICP-AES measurements. As displayed in Table S1, Ru contents vary from 2.9 wt% to 5.1 wt% for these samples, in which the sample with 3.8 wt% Ru was investigated in detail in this work (denoted as Ru/Ni-NiO@C in the main text). Ru/NiO@C ($300 \text{ }^\circ\text{C}$), Ru/Ni-NiO@C-500, and Ru/Ni-NiO@C-600 were prepared under a similar protocol except for the pyrolysis temperatures ($300, 500, 600 \text{ }^\circ\text{C}$, respectively). As reported in the literature, the morphology of MOFs-derived material is tightly correlated with the carbonization temperatures, which is

further determined by the TGA. High-temperature ($>600 \text{ }^\circ\text{C}$) pyrolysis usually makes the MOFs skeleton prone to collapse. We then carried out a TGA to reveal the decomposition of organic linker dependence on carbonization temperatures. The thermal behavior of Ni-MOF under N_2 atmosphere is presented in Fig. 1(b), the weight loss of Ni-MOF up to $300 \text{ }^\circ\text{C}$ is mainly caused by the evaporation of absorbed water and DMF molecule. Subsequently, a significant mass loss in $300\text{--}400 \text{ }^\circ\text{C}$ is originated from both the decomposition of organic ligands and the transformation of Ni^{2+} to NiO. In the temperature range of $400\text{--}800 \text{ }^\circ\text{C}$, the weight loss is corresponding to the reduction of NiO to metallic Ni by the carbon [20]. As evidenced by the TGA, we chose to carbonize MOFs at $400 \text{ }^\circ\text{C}$. After annealing, the XRD (Fig. 1c) signals of NiO (JCPDS: 47-1049) can be detected at low temperature ($300 \text{ }^\circ\text{C}$). Moreover, the diffraction peaks at 44.5° , 51.8° , and 76.4° are indexed to the metallic Ni (JCPDS: 04-0850) at higher annealing temperatures ($400\text{--}600 \text{ }^\circ\text{C}$) [20]. No diffraction peaks being ascribable to Ru can be discernible, indicating that Ru in Ru/Ni-NiO@C is amorphous.

3.2. Nickel/oxygen vacancies characterized by Raman, EPR and XPS

We performed multiple spectroscopic characterizations to achieve information pertaining to the detailed structure of Ru/Ni-NiO@C. Raman spectroscopy is a powerful tool to probe the metal-oxygen bonding situation and structural defects of nanomaterials [29]. As shown in Fig. 2(a), Raman spectrum shows broad D ($\sim 1340 \text{ cm}^{-1}$) and G ($\sim 1586 \text{ cm}^{-1}$) bands of carbon, which corresponds to defective/disorder and graphitic carbon. The I_D/I_G values of Ni-NiO@C, Ru/Ni-NiO@C, Ru/Ni-NiO@C-500 and Ru/Ni-NiO@C-600 are 0.95, 1.03, 0.95, and 0.97. The higher I_D/I_G band intensity ratio of Ru/Ni-NiO@C reveals the presence of more defect sites in the carbon support, which can introduce diversified active sites [30,31]. Note that the insufficient graphitization of organic ligands at $300 \text{ }^\circ\text{C}$ makes the D- and G-band of Ru/NiO@C ($300 \text{ }^\circ\text{C}$) invisible. Besides, the Ni-NiO@C Raman spectra show the peaks at $520, 770,$ and 900 cm^{-1} . The first peak at 520 cm^{-1} is relative to one-phonon (1P) longitudinal optical (LO) of NiO vibrational modes, while the other peaks at 770 and 900 cm^{-1} correspond to two-phonon (2P) transverse optical $2P_{\text{TO}}$, $2P_{\text{TO+LO}}$, respectively [29]. We can see that

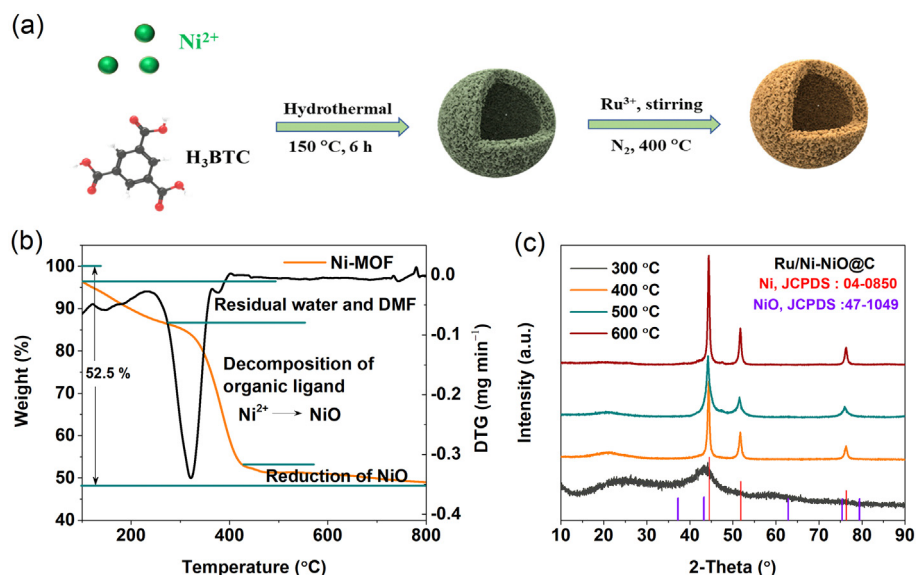


Fig. 1. (a) Schematic illustration of the synthesis of Ru/Ni-NiO@C. (b) TGA measurement of Ru/Ni-NiO@C. (c) XRD patterns of as-synthesized samples at different temperatures.

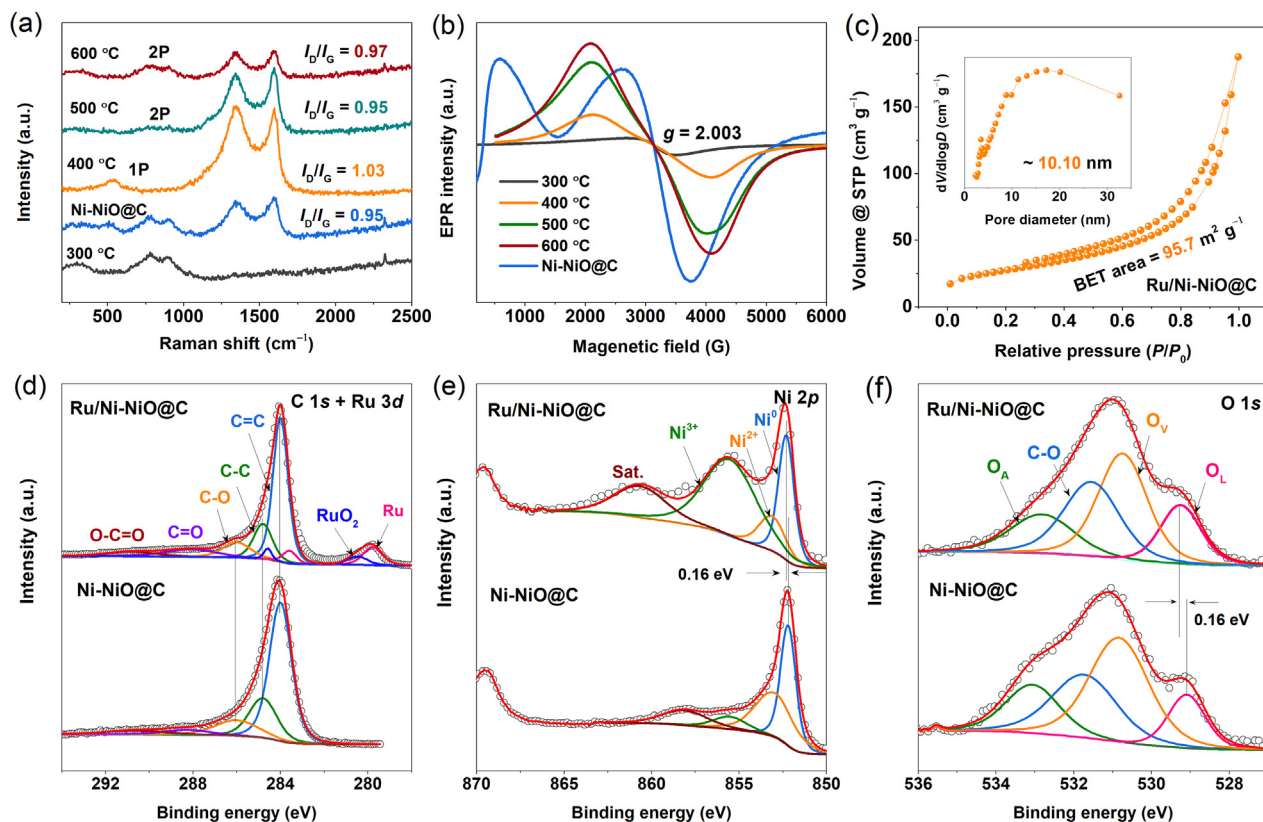


Fig. 2. (a) Raman spectra and (b) EPR spectra of as-synthesized samples at different temperatures. (c) N_2 adsorption/desorption isotherm with the inset showing the corresponding pore size distribution of Ru/Ni-NiO@C. High-resolution XPS spectra of (d) C 1s + Ru 3d, (e) Ni 2p, and (f) O 1s regions in Ru/Ni-NiO@C and Ni-NiO@C, respectively.

Ru/NiO@C (300 °C), Ru/Ni-NiO@C-500, and Ru/Ni-NiO@C-600 show two peaks at 770 and 900 cm^{-1} , while the Ru/Ni-NiO@C Raman spectrum shows one peak at 520 cm^{-1} . According to the precedent studies, $1P_{LO}$ mode (at 520 cm^{-1}) is Raman inactive in a perfect single crystal, but surface effect or the presence of vacancy makes it visible [23]. In addition, in-depth studies have revealed that Ni vacancy concentration dominates the intensity of $1P_{LO}$ mode [23,32]. However, when $1P_{LO}$ becomes more pronounced due to the presence of nickel vacancies, two bands of $2P_{TO}$ (770 cm^{-1}) and $2P_{TO+LO}$ (900 cm^{-1}) will be broader and even disappear [33]. The existence of $1P_{LO}$ mode can be attributed to large amounts of innate nickel vacancies in Ru/Ni-NiO@C. Abundant Ni vacancy-induced defects in the interface of Ni-NiO heterostructure can provide more active sites [23]. Oxygen vacancies were well reported as they are the common theme in metal oxides and particularly relevant for promoting catalytic activities [34]. We then resorted to the EPR for direct oxygen vacancies identification (Fig. 2b). The apparent symmetrical signals at $g = 2.003$ correspond to oxygen vacancies of the samples except for Ru/NiO@C [35]. A monotonic increase in the oxygen vacancy concentration is observed with increasing annealing temperature. Compared with Ni-NiO@C, the EPR intensity of Ru/Ni-NiO@C was attenuated somewhat, which possibly due to the Ru-species effectively occupied some of oxygen defect sites. The vacancies (oxygen-vacancy and nickel-vacancy) introduced in Ru/Ni-NiO@C can substantially modify its electronic properties, leading to its enhanced HOR activity [36]. Analysis of Brunauer-Emmett-Teller (BET) adsorption-desorption isotherm indicates that the specific surface area of Ru/Ni-NiO@C is 95.7 $m^2 g^{-1}$. Additionally, the pore size distribution of Ru/Ni-NiO@C is 10.10 nm, indicating that it is a mesoporous material. These mesopores act as isolators, which can

prevent Ru NPs from stacking and increase the access of active sites (Fig. 2c) [37].

The depth profile XPS elucidated the surface chemical constitution and electron state of the samples. XPS analysis of Ru/Ni-NiO@C confirms the presence of C, O, Ni, and Ru elements (Fig. S1). The deconvoluted high-resolution XPS spectra of C 1s + Ru 3d regions in Fig. 2(d) display the main sharp and strong peaks at C=C (284.0 eV), C-C (284.8 eV), and C-O (286.1 eV) and used as calibration standard [38]. Meanwhile, the Ru $3d_{5/2}$ core level can be divided into two groups of peaks at 280.0, 283.7 eV (Ru^0 3d) and 280.5, 284.5 eV (RuO_2 3d), respectively. As shown in Fig. 2(e), the high-resolution Ni 2p spectra of Ru/Ni-NiO@C are disassembled into four peaks at 852.4, 853.1, 855.7, and 861.1 eV, which are ascribed to metallic Ni, Ni^{2+} , Ni^{3+} , and satellite peaks, respectively, suggesting the part of Ni^{2+} was successfully reduced to Ni^0 through the carbonization process [23]. XPS analysis also provides the foremost evidence of the coexistence of Ni^{2+} and Ni^{3+} . The presence of Ni^{3+} suggests Ni vacancies are successfully incorporated into the lattice of Ru/Ni-NiO@C during annealing. The oxidation of Ni^{2+} to Ni^{3+} to maintain charge balance of near-surface Ni vacancies echoes the above Raman results [23]. Interestingly, the XPS peak belonging to Ni^0 in Ru/Ni-NiO@C illustrates a positive shift (0.16 eV) compared to Ni-NiO@C, indicating a strong electronic effect between Ni and Ru species [39]. The XPS analysis further demonstrates a strong electronic interaction occurring between Ru and Ni-NiO@C, which Ru could effectively reshape the electronic structure of Ni species. Furthermore, we also examined the oxygen vacancies formation by the O 1s core level XPS spectra of Ru/Ni-NiO@C (Fig. 2f). The asymmetric O 1s peak can be deconvoluted into four peaks existing at 529.3, 530.7, 531.5, and 532.8 eV, conforming to lattice oxygen (O_L), oxygen vacancies

(O_V), C–O bond, and surface adsorbed oxygen species (O_A), respectively [40]. Clearly, a negative binding energy (BE) shift (ca. 0.16 eV) is observed for O 1s in Ni–NiO@C compared with Ru/Ni–NiO@C, indicating that electrons are transferred to the neighboring oxygen vacancies [40]. According to the integrated peak areas, the concentration of oxygen vacancies [$S_{\text{oxygen vacancy}} / (S_{\text{oxygen vacancy}} + S_{\text{lattice oxygen}})$] of Ru/Ni–NiO@C (0.69) is lower than Ni–NiO@C (0.76), which is likely that the Ru-species occupied some of defects induced by O vacancies in Ru/Ni–NiO@C. These results match well with EPR analyses. Combining the results mentioned above, it is clear that an active nanostructure is formed with Ru NPs coupled with nickel/oxygen vacancies, which can enhance electronic interaction and accelerate interfacial electron transfer rate between Ru and Ni–NiO@C [41,42].

3.3. SEM and TEM characterizations

The morphological evolution of the Ru/Ni–NiO@C composite was tracked by SEM. As depicted in Fig. 3(a), Ru/Ni–NiO@C shows the typical microspherical hollow morphology preserved from Ni–MOF (Fig. S2), which can furnish large free space for Ru loading. The average diameter of Ru/Ni–NiO@C was estimated to be approximately 1 μm . Notably, the microsphere's surface covered a large quantity of nanoparticles, thus forming a hierarchical order at micro/nano levels, which also well demonstrated the effectiveness of our synthetic strategy toward supported nanoparticles with high homogeneity. Such micro/nano superstructure favors to provide a large fraction of electrochemical accessible surface area [43]. Further, the hierarchical hollow nature was also confirmed by the TEM image (Fig. 3b), evident from the bright-dark contrast variation between edges and centers. The statistical results of about 200 Ru and Ni–NiO NPs concluded that the average particle size is approximately 1.28 nm for Ru NPs and 9.15 nm for Ni–NiO NPs (Figs. S3 and S4). From the high-resolution TEM (HRTEM) image (Fig. 3c), Ru, Ni, and NiO phases are found on the microspherical surface. The lattice distance of one NP is about 0.18 nm, which can be indexed to (200) plane of cubic Ni. The well-resolved lattice fringes with the inter-planar distance of about 0.21 and 0.16 nm are assigned to NiO (200) plane and metallic Ru (102) plane, respectively. The existence of Ni and NiO in Ru/Ni–NiO@C was further supplemented by the selected area electron diffraction (SAED) pattern (Fig. S5a). The prominent electron diffraction rings or aggregated dots belong to Ni (200) and NiO (200) phases. At the same time, Ru is amorphous, and no evident diffraction ring is observed, consistent with XRD results. Moreover, the HRTEM image also demonstrates several curved graphene layers from the carbon frameworks, which serve as protective shells that contribute to prevention of coalescence of Ru NPs during annealing

[44]. The carbon-coated structure is formed during the pyrolysis of MOF. Undoubtedly, this carbon-coated structure can effectively improve the electrical conductivity of the transition metal nanoparticles and protect the active centers from corrosion by alkalis [20,45]. As shown in Fig. 3(d) and Fig. S5(b), the high-angle annular dark-field scanning transmission electron microscopy (HAADF-STEM) image and corresponding elemental mappings of Ru/Ni–NiO@C further corroborate the coexistence of C, O, Ni, and Ru in the entire sample.

3.4. Electrocatalytic HOR in alkaline electrolytes

The HOR electrocatalytic activity of as-prepared catalysts was first probed by using the rotating disk electrode (RDE) technique in H_2 -saturated 0.1 M KOH electrolyte. The reversible hydrogen electrode (RHE) calibration was performed before measurements (Fig. S6), and electrochemical data were presented with iR -corrected (Fig. S7). Initially, we performed quick screening experiments according to the TGA results, therefore the annealing temperature is fixed at 400 $^\circ\text{C}$ to optimize the Ru loading on the catalytic activity of Ru/Ni–NiO@C. As shown in Fig. 4(a), electrocatalytic performance of Ru/Ni–NiO@C varied with the change of Ru loading from 2.9 to 5.1 wt%, in which the sample with 3.8 wt% Ru (denoted as Ru/Ni–NiO@C) loading stands out as the best HOR catalyst among the series, showing that the appropriate Ru loading is vital for successful Ru utilization. Tafel plots in Fig. 4(b) also validate the fastest HOR kinetics on Ru/Ni–NiO@C. Fig. 4(c) reveals that the kinetic current density (j_k) at 50 mV and electrochemical active surface area (ECSA)-normalized exchange current density ($j_{0,s}$) values show parabolic behaviors, where the maximum values of $j_k @ \eta = 50 \text{ mV}$ (32.61 mA cm^{-2}) and $j_{0,s}$ (0.084 mA cm^{-2}) from the micro-polarization region (-10 to 10 mV) by linear fitting through the Butler-Volmer equation (Fig. S8) are obtained with 3.8 wt% Ru loading is chosen as the basis for the subsequent experiments.

The catalyst performance depends on the phase and Ni/NiO ratio of the resultant products governed by the annealing temperature. We utilized XPS analysis to investigate the surface chemical composition of the samples. As shown in Fig. S9(a), Ru/NiO@C (300 $^\circ\text{C}$) does not have metallic Ni in its structure because the carbonization rate is relatively low at 300 $^\circ\text{C}$, which is in line with TGA and XRD results. The Ru/NiO@C (300 $^\circ\text{C}$) sample, featuring only the NiO phase, shows nearly inactive toward HOR, demonstrating the promotional effect of metallic Ni on uplifting the intrinsic activity of HOR (Fig. 4d–f). To verify the pivotal role of the Ni/NiO ratio in the HOR activity, we analyzed Ni/NiO ratio quantitatively in developed catalysts via XPS. An increase of metallic Ni can be observed with the annealing temperature is elevated from 400 to 600 $^\circ\text{C}$ (Fig. S9a). The XPS survey spectra demonstrated the coexistence

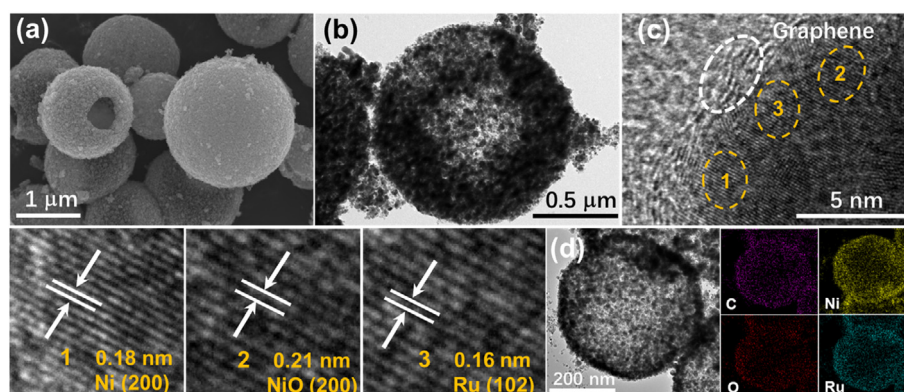


Fig. 3. (a) SEM image, (b) TEM image, (c) high-resolution TEM images, and (d) HAADF-STEM image and corresponding elemental mappings of Ru/Ni–NiO@C.

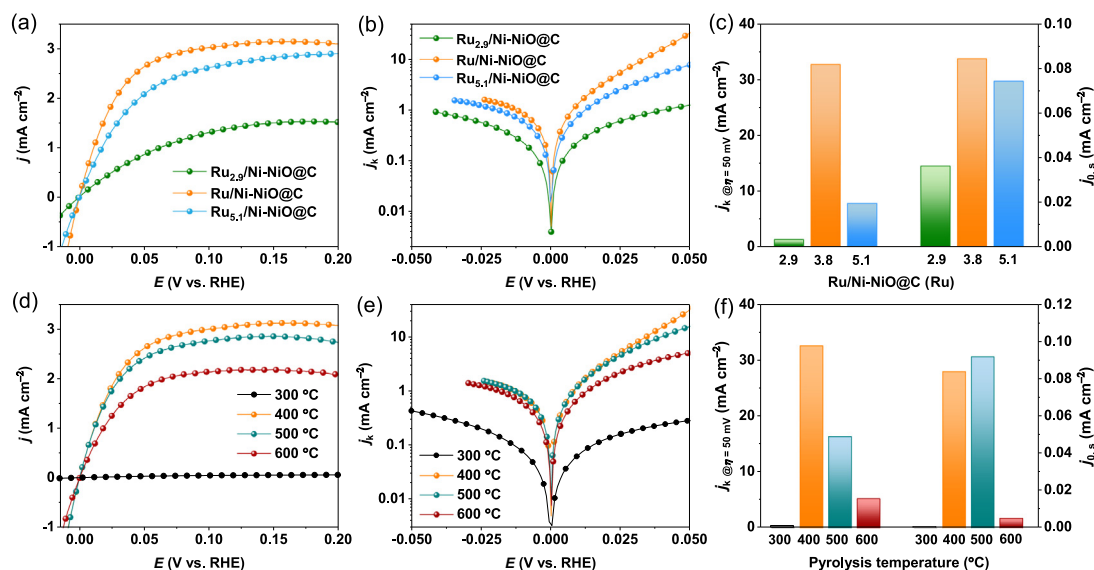


Fig. 4. (a) HOR polarization curves of Ru/Ni-NiO@C at different loading of Ru species. (b) HOR/HER Tafel plots of j_k . (c) Comparison of the j_k at 50 mV and ECSA normalized $j_{0.5}$ ($j_{0.5}$) of different studied catalysts. (d) HOR polarization curves. (e) HOR/HER Tafel plots of j_k . (f) comparison of the j_k at 50 mV and $j_{0.5}$ of as-synthesized samples at different temperatures.

of the Ni and NiO phase in the samples, and Ni/NiO ratio is quantitatively determined to be 1.6, 2.3, and 3.5 for Ru/Ni-NiO@C-400, Ru/Ni-NiO@C-500, and Ru/Ni-NiO@C-600, respectively (Table S2). Correspondingly, anodic current densities were significantly decreased in the RDE voltammogram with the Ni/NiO ratio increase. The result demonstrates Ru/Ni-NiO@C annealed at 400 °C possesses an optimal Ni/NiO ratio, which is responsible for enhancing HOR. The relationship between Ni/NiO ratio and HOR activity is further visualized in Fig. S10.

The surface vacancies of electrocatalysts may induce positive effects on an electrochemical reaction. We next tried to quantify the nickel/oxygen vacancies in NiO species by XPS to unveil the vacancy-activity relationship. The content ratio was calculated based on the proportion of its fitting peaks [23]. The XPS survey spectra demonstrated the successful introduction of nickel/oxygen vacancies, with a content Ni^{3+} ratio of 82.2%, 59.9%, 62.2%, and 49.1%, while the content ratio of oxygen vacancies is 64.4 %, 68.1%, 70.2 %, and 77.1 % for Ru/NiO@C-300, Ru/Ni-NiO@C-400, Ru/Ni-NiO@C-500, and Ru/Ni-NiO@C-600, respectively (Fig. S9b and Table S2). It can be seen the general decrease in nickel vacancies concentration but an increase in oxygen vacancies concentration with the increase of annealing temperature. Then, we investigated the effect of nickel/oxygen vacancies concentration on the HOR performance. The linear sweep voltammetry (LSV) curves in Fig. 4(d) show that the HOR anodic current density was apparent attenuation when the pyrolysis temperature was increased from 400 to 600 °C. Hence, the ideal performance at 400 °C can be ascribed to the synergistic optimization of both nickel and oxygen vacancies concentration. Besides, the HOR performance parameters of all samples were given in Table S3.

HBE has been considered as a key descriptor to evaluate HOR activity [10,15,46]. The hydrogen under-potential deposition (H_{upd}) peaks in a cyclic voltammogram (CV) directly correlate with HBE. The peak at the lower potential in the H_{upd} region corresponds to the weaker metal-H bond strength. In comparison, the one at higher potential relates to the stronger metal-H bond strength [47], and the weaker HBE is more conducive to HOR [48]. Previous studies demonstrated that high HOR performance generally depends on two factors. Firstly, because of the stronger electron-transfer interaction, the adsorption capability of small

adsorbates (such as CO_{ad} and H_{ad}) on catalysts surface would be weakened, which effectively promotes alkaline HOR performance [15,49]. On the other hand, Xie et al. designed a new Rh@Pt_x with surface defects, pointing out the importance of structural defects toward HOR activity [50]. In Fig. 5(a), the CV curves of Ru/Ni-NiO@C were tested in N_2 -saturated 0.1 M KOH with reference measurements of Ni-NiO@C, Pt/C, and Ru/C for comparison. The H_{upd} peak potential of Ru/Ni-NiO@C (0.17 V vs. RHE) is more negative than that of Pt/C (0.30 V vs. RHE), possibly due to the presence of surface vacancies and weakened HBE [50], reflecting the Ru/Ni-NiO@C possesses the higher HOR activity than Pt/C. In contrast, Ni-NiO@C and benchmark Ru/C show unremarkable H_{upd} peaks, revealing the strong electronic interaction between Ru and Ni-NiO@C species can weaken the HBE [12,49]. Fig. 5(b) shows the HOR polarization curves of the catalysts in H_2 -saturated electrolytes, it is apparent that Ru/Ni-NiO@C achieves the highest anodic current density. And the onset potential of HOR on Ru/Ni-NiO@C is as low as 0 V (vs. RHE), highlighting its remarkable energetic for alkaline HOR [8]. Control experiment conducted in N_2 -saturated electrolyte exhibits nearly inactive (Fig. S11), demonstrating H_2 is a reactant for HOR. The steady-state limiting current density (j_{lim}) indicates the maximum diffusion current density in HOR during RDE measurement, which should be a fixed value in theory in a particular concentration solution and at a certain rotate speed. However, j_{lim} is continuously variable and lies below the theoretical value with the same catalyst, electrode, and rotating speeds in experiments. The differences in the j_{lim} between measurements reveal the existence of several factors (e.g., catalyst loading, solution concentration, H_2 flow rate, and gas tightness) that affect the electrochemical kinetics. Therefore, we provided experimental evidence regarding the effect of the above four factors on the measured j_{lim} for HOR by using 20 wt% commercial Pt/C as a catalyst (Figs. S12 and S13). The results show that catalyst loading is regarded as the critical factor, which impacts the j_{lim} of HOR in this work. Fig. 5(c) shows the Tafel plots, demonstrating a quicker HOR kinetics of Ru/Ni-NiO@C. Next, we studied the polarization curves of Ru/Ni-NiO@C at different rotating speeds from 400 to 1600 r min^{-1} , where the current density increases with increasing rotation rate due to the promoted mass transport (Fig. S14). As plotted in Fig. 5(d), the j_0 on as-prepared catalysts

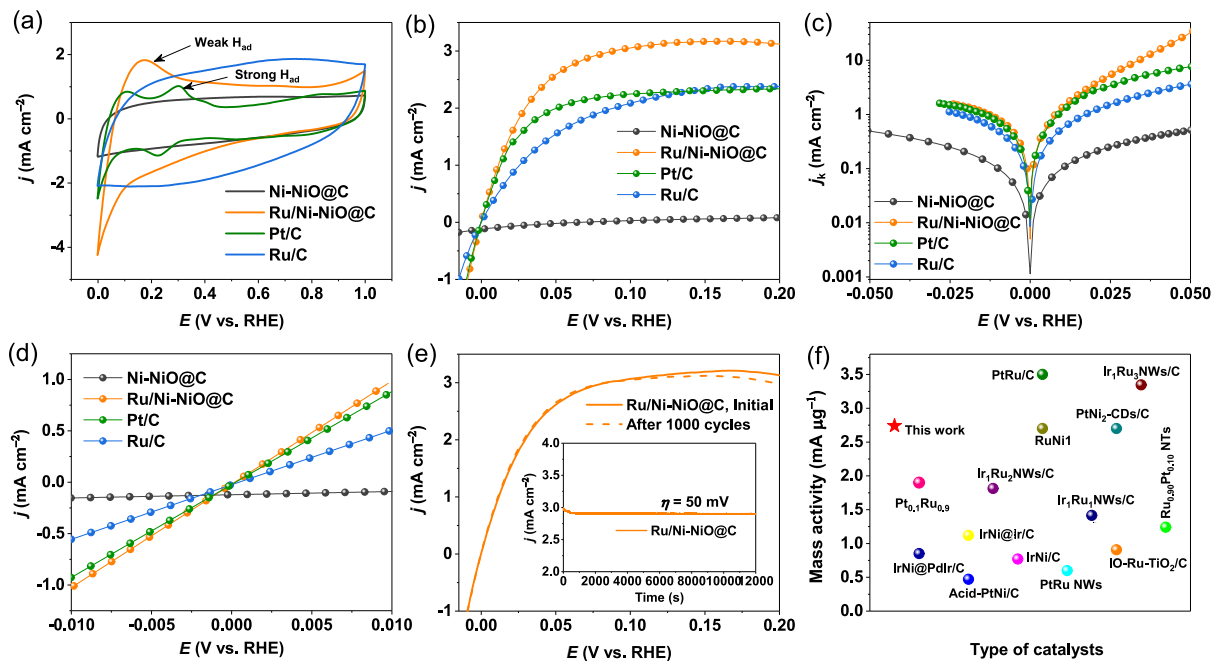


Fig. 5. (a) CV curves in N_2 -saturated 0.1 M KOH at a scan rate of 50 mV s^{-1} . (b) HOR polarization curves. (c) Representative HOR/HER Tafel plots. (d) Linear current potential region around the equilibrium potential for the HOR on studied catalysts. (e) Accelerated durability test and chronoamperometric response of Ru/Ni-NiO@C. (f) Comparison of mass activity at 50 mV with other recently reported excellent HOR catalysts (horizontal axis: type of HOR catalysts).

is evaluated from linear fitting of micropolarization regions (-10 to 10 mV), in which the slope is proportional to j_0 [51]. We show the $j_{0,s}$ and find that the $j_{0,s}$ is 0.084 mA cm^{-2} for Ru/Ni-NiO@C, comparable to Pt/C (0.095 mA cm^{-2}) catalyst, implying good intrinsic HOR activity of Ru/Ni-NiO@C (Table S3). Fig. 5(e) shows the polarization curves of Ru/Ni-NiO@C before and after 1000 CV cycles, the two polarization curves almost overlap. Moreover, we also assessed the stability of Ru/Ni-NiO@C by chronoamperometry at $\eta = 50 \text{ mV}$, which delivers a stable current density without degradation throughout the test. As demonstrated in Fig. S15, Ru/Ni-NiO@C-After catalyst still preserves its pristine morphology. Moreover, we find that the Ru/Ni-NiO@C-After still has Ru, Ni^0 , Ni^{2+} , Ni^{3+} , and O_v signals, and the peak intensities were similar to Ru/Ni-NiO@C even after the long-term stability test (Fig. S16). In conclusion, these results clearly indicate that our developed catalyst bears a robust surface structure that protects the active centers from alkali corrosion during HOR. Apart from kinetics current and exchange current evaluation of catalysts, the metal loading normalized data comparison gives a more accurate picture of catalyst activity. The mass activity of Ru/Ni-NiO@C is calculated to be $2.79 \text{ mA } \mu\text{g}_{\text{Ru}}^{-1}$, exceeding most of the previous electrocatalysts (Fig. 5f and Tables S3 and S4).

As Ru is susceptible to oxidation in the hydrogen adsorption/desorption potential region, it is not suitable to calculate the ECSA by measuring the charge associated with the H_{upd} region. Therefore, we performed CO stripping voltammetry to measure the ECSA value of samples. As shown in Fig. 6, the ECSA of Ru/Ni-NiO@C was estimated to be $52.9 \text{ m}^2 \text{ g}^{-1}$, higher than Pt/C ($48.1 \text{ m}^2 \text{ g}^{-1}$) and Ru/C ($15.8 \text{ m}^2 \text{ g}^{-1}$). The ECSAs of other catalysts were summarized in Table S3. Higher ECSA implies more active sites for catalytic reactions, which favors the close contact of reactants with electrolyte [52]. The excellent HOR activity of Ru/Ni-NiO@C motivated our investigation for its hydrogen evolution reaction (HER). Ru/Ni-NiO@C shows an excellent HER activity and stability, and is among the best precious metal based electrocatalysts (Figs. S17 and S18 and Table S5).

3.5. HOR enhancement mechanism

Systematic theories and operando experiments have demonstrated that HBE and OHBE are the descriptors to precisely interpret the underlying causes of activity enhancement of alkaline HOR [8,11]. Considering that OH_{ad} species can accelerate the remove of CO_{ad} species intermediate on metal surface, and the CO stripping potential is correlated directly with the strength of OH^- adsorption [8,15]. Further, the electronic effect or special surface structure of Ru/Ni-NiO@C can decrease H_{ad} intermediates binding energy and the adsorption strength of CO_{ad} [49]. Thus, CO-stripping experiments were further conducted to monitor the OH binding of the catalysts, and their results were recorded in Fig. 6. In Fig. 6(a and b), the CO oxidation peak of Ru/Ni-NiO@C is about 0.63 V , which can be seen clearly that Ru/Ni-NiO@C exhibits the strongest OH^- adsorption among these materials [53]. In Fig. 6 (c and d), the CO oxidation peaks of Pt/C and Ru/C are at 0.74 and 0.73 V . Previous studies investigating the sluggish HOR kinetics of Pt concluded that its weak OH_{ad} binding in alkaline [8,54]. Our CO stripping results indicate that enhanced OH_{ad} on Ru/Ni-NiO@C might account for the enhancement of alkaline HOR performance. As revealed by the CV behavior, the weakening of H_{ad} binding energy is due to the incorporation of Ru yields an electronic effect at the Ru and Ni-NiO@C interface and surface defects induced by Ni/O vacancies, as XPS showed [15,50,55]. To bring theoretical insights into the HOR mechanism of Ru/Ni-NiO@C and pinpoint the active sites, we conducted DFT calculations. Fig. S19 shows the optimal structure model of Ru/Ni-NiO@C (details in Computational methods). The differential charge density of Ru/Ni-NiO@C shows that there is overt charge depletion around Ni and charge accumulation around Ru, again interpreting the strong electronic interaction between Ru and Ni species (Fig. 7a). We examined various possible sites on Ru, Ni, and NiO position in Ru/Ni-NiO@C to compute their HBE and OHBE (Figs. S20 and S21). Fig. 7(b) shows the optimal adsorption sites of H_{ad} , the calculated HBE on Ru sites was -0.41 eV , very close to the binding energy on Pt (111) (-0.40 eV), and eventually results in the theoretical optimal value

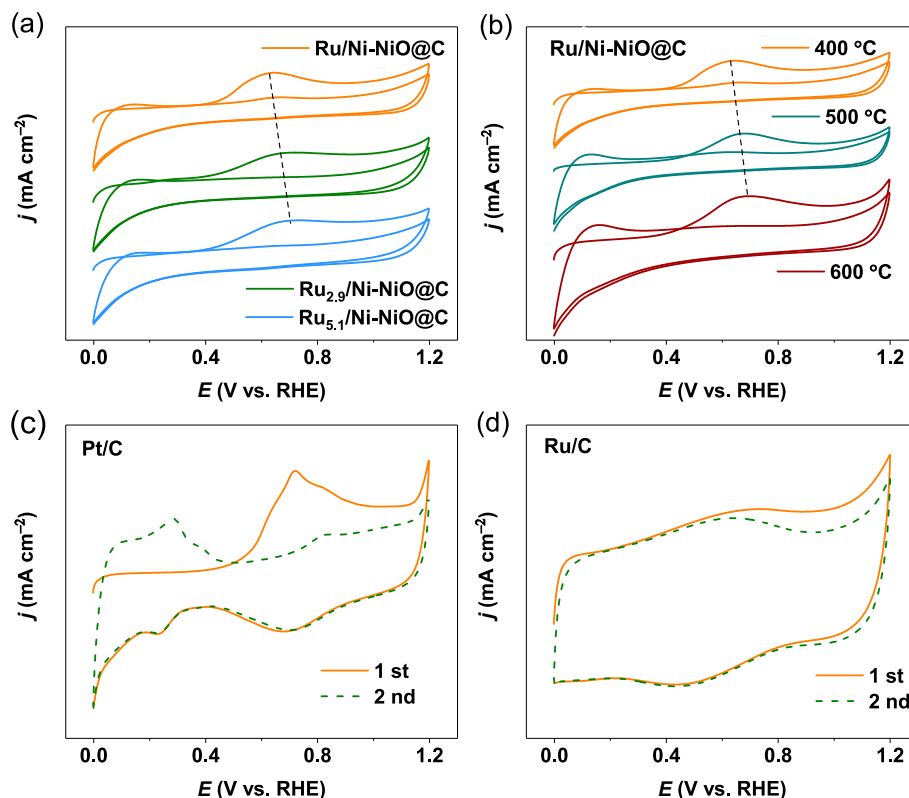


Fig. 6. CO stripping curves in CO-saturated 0.1 M KOH of different studied catalysts. (a) Ru/Ni-NiO@C, Ru_{2.9}/Ni-NiO@C, and Ru_{5.1}/Ni-NiO@C. (b) Different temperatures of Ru/Ni-NiO@C. (c) Pt/C. (d) Ru/C.

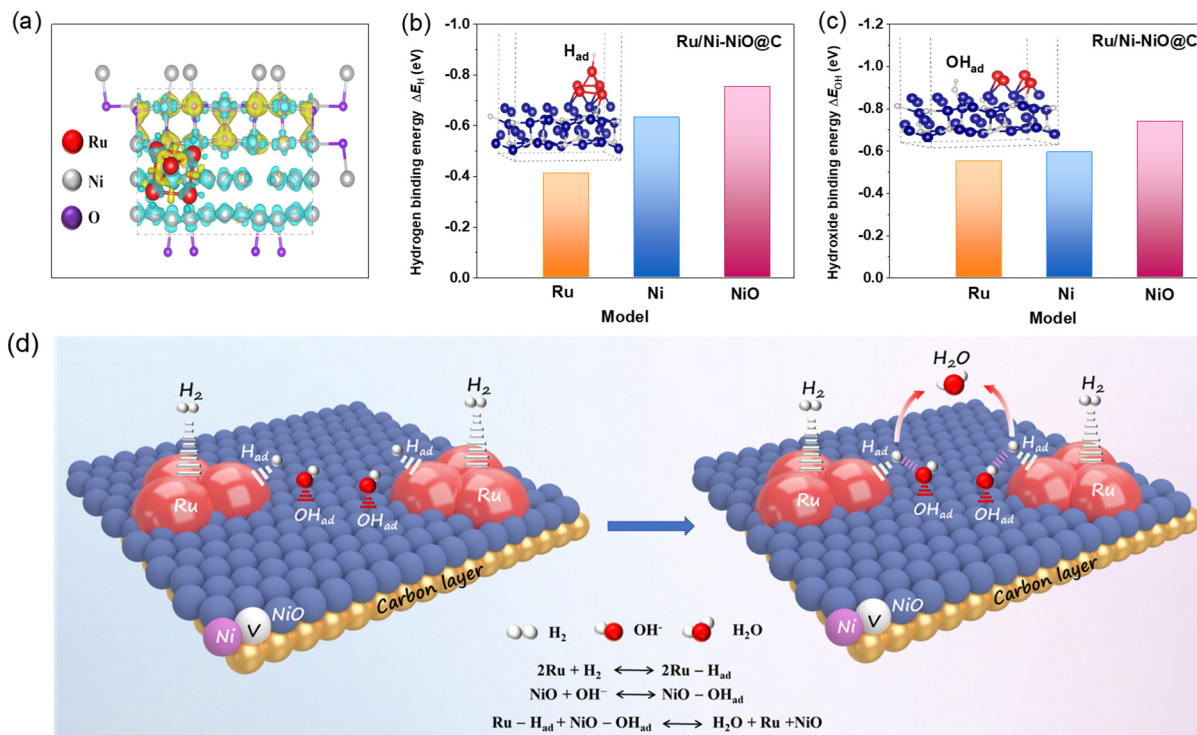


Fig. 7. (a) Charge-density distribution of the Ru/Ni-NiO@C model. The yellow and blue colors represent charge accumulation and depletion, respectively. (b) Calculated HBE of Ru, Ni, and NiO in the Ru/Ni-NiO@C model. The inset illustrates optimized hydrogen adsorption configuration on Ru sites. (c) Calculated OHBE of Ru, Ni, and NiO in the Ru/Ni-NiO@C model. The inset illustrates optimized hydroxide adsorption configuration on NiO sites. (d) HOR mechanism in alkaline medium at Ru/Ni-NiO@C electrode.

of ΔG_{H^+} ($\Delta G_{H^+} = 0$ eV) [7]. Therefore, the much-weakened HBE on Ru sites is a synergistic electronic effect between Ru and Ni species, which tremendously facilitates the critical Volmer step, leading to the HOR enhancement [17]. Fig. 7(c) presents optimal OH_{ad} sites on NiO with a binding energy of -0.74 eV, giving a very similar OHBE with Pt(111) (-0.87 eV) model compared with Ru (-0.55 eV) and Ni (-0.59 eV) [7]. Such a strengthened OH_{ad} adsorptive behavior results from the surface structure containing nickel/oxygen vacancies, contributing to capturing OH^* species on the NiO surface [17], thereby promoting the Volmer step during alkaline HOR process and enabling Ru/Ni-NiO to follow the bifunctional mechanism at the Ru and Ni-NiO@C interface, with adsorption of H_{ad} on Ru and OH_{ad} on NiO sites. Besides, Ni arguably plays an auxiliary role in accelerating the charge transport [23]. Thus, a bifunctional mechanism that balanced both optimal HBE and OHBE is proposed for Ru/Ni-NiO@C in alkaline medium, as shown in Fig. 7(d).

Based on the characterizations and experimental results, the augmenting HOR activity of Ru/Ni-NiO@C arises from the following aspects: (1) The flexible cavities and hierarchically porous structure favor the mass/charge transportation [56]. (2) Strong electronic interactions between Ru species and Ni-NiO@C support can reduce the interfacial impedance and expedite HOR kinetics [57]. (3) Annealing induces Ni and O vacancies in Ru/Ni-NiO@C to enhance electronic conduction and generate additional catalytically active sites [23,58]. (4) High conductivity of carbon and metal Ni facilitates electron transportation [20,23]. (5) Synergistic interplay of both optimal H_{ad} and OH_{ad} on Ru/Ni-NiO@C surface substantially promotes the key Volmer step [7,49].

4. Conclusions

In summary, we reported a rational manipulation strategy to construct Ru/Ni-NiO@C electrocatalyst via a MOF-engaged replacement-pyrolysis method, in which Ru NPs are coated onto the hollow Ni-NiO@C, forming an intimately contacted superstructure. Utilizing the mutual interaction between metal Ru and vacancies-rich Ni-NiO@C support achieves not only desirable dispersity but also regulated interfaces. Annealing treatment at 400 °C induces vacancies in Ru/Ni-NiO@C, which provides additional insights in the reactivity of the active sites. The vacancies can act as a “claw” to capture and couple firmly with Ru species, thus optimize the charge transfer and catalytic active sites. DFT calculations reveal that electronic interaction between Ru and Ni-NiO@C, together with vacancy-rich NiO species contribute to the optimal HBE and enhanced OHBE, collectively shifting the HOR activity toward the vertex of the volcano plot. Specifically, the HOR mass activity of Ru/Ni-NiO@C is 2.79 mA $\mu\text{g}_{\text{Ru}}^{-1}$, which is 7.75 times higher than that of Pt/C catalyst. The Ru/Ni-NiO@C also shows high durability without degradation over 1000 cycles. This work presents a facile scenario to construct catalytic sites using vacancy defects. It offers a promising approach for cost-effective precious-metal-based catalysts in the field of hydrogen oxidation.

Declaration of competing interest

The authors declare that they have no known competing financial interests or personal relationships that could have appeared to influence the work reported in this paper.

Acknowledgments

This work has been supported by the National Natural Science Foundation of China (21965005), the Natural Science Foundation of Guangxi Province (2018GXNSFAA294077, 2021GXNSFAA076001), the Project of High-Level Talents of

Guangxi (F-KA18015), and the Guangxi Technology Base and Talent Subject (GUIKEAD18126001, GUIKE AD20297039).

Appendix A. Supplementary data

Supplementary data to this article can be found online at <https://doi.org/10.1016/j.jechem.2022.06.011>.

References

- [1] J. Zheng, Z. Zhuang, B. Xu, Y. Yan, *ACS Catal.* 5 (2015) 4449–4455.
- [2] G. Zhao, J. Chen, W. Sun, H. Pan, *Adv. Funct. Mater.* 31 (2021) 2010633.
- [3] Y. Xue, L. Shi, X. Liu, J. Fang, X. Wang, B.P. Setzler, W. Zhu, Y. Yan, Z. Zhuang, *Nat. Commun.* 11 (2020) 5651.
- [4] L. Su, D. Gong, Y. Jin, D. Wu, W. Luo, *J. Energy Chem.* 66 (2022) 107–122.
- [5] Z. Zhang, H. Liu, L. Ni, Z.-L. Zhao, H. Li, *J. Energy Chem.* (2022), <https://doi.org/10.1016/j.jechem.2022.04.043>.
- [6] T. Zhao, D. Xiao, Y. Chen, X. Tang, M. Gong, S. Deng, X. Liu, J. Ma, X. Zhao, D. Wang, *J. Energy Chem.* 61 (2021) 15–22.
- [7] Y. Yang, X. Sun, G. Han, X. Liu, X. Zhang, Y. Sun, M. Zhang, Z. Cao, Y. Sun, *Angew. Chem. Int. Ed.* 58 (2019) 10644–10649.
- [8] Y. Duan, Z.-Y. Yu, L. Yang, L.-R. Zheng, C.-T. Zhang, X.-T. Yang, F.-Y. Gao, X.-L. Zhang, X. Yu, R. Liu, H.-H. Ding, C. Gu, X.-S. Zheng, L. Shi, J. Jiang, J.-F. Zhu, M.-R. Gao, S.-H. Yu, *Nat. Commun.* 11 (2020) 4789.
- [9] W. Sheng, M. Myint, J.G. Chen, Y. Yan, *Energy Environ. Sci.* 6 (2013) 1509–1512.
- [10] L. Fu, Y. Li, N. Yao, F. Yang, G. Cheng, W. Luo, *ACS Catal.* 10 (2020) 7322–7327.
- [11] Y. Qiu, L. Xin, Y. Li, I.T. McCrum, F. Guo, T. Ma, Y. Ren, Q. Liu, L. Zhou, S. Gu, M.J. Janik, W. Li, *J. Am. Chem. Soc.* 140 (2018) 16580–16588.
- [12] Y. Yang, X. Shao, S. Zhou, P. Yan, T.T. Isimjan, X. Yang, *ChemSusChem* 14 (2021) 2992–3000.
- [13] Y. Yang, Q. Dai, L. Shi, Y. Liu, T.T. Isimjan, X. Yang, *J. Phys. Chem. Lett.* 13 (2022) 2107–2116.
- [14] B. Tang, X. Yang, Z. Kang, L. Feng, *Appl. Catal. B: Environ.* 278 (2020) 119281.
- [15] Y. Wang, G. Wang, G. Li, B. Huang, J. Pan, Q. Liu, J. Han, L. Xiao, J. Lu, L. Zhuang, *Energy Environ. Sci.* 8 (2015) 177–181.
- [16] S. Deng, X. Liu, X. Guo, T. Zhao, Y. Lu, J. Cheng, K. Chen, T. Shen, Y. Zhu, D. Wang, *J. Energy Chem.* 54 (2021) 202–207.
- [17] F. Yang, X. Bao, P. Li, X. Wang, G. Cheng, S. Chen, W. Luo, *Angew. Chem. Int. Ed.* 58 (2019) 14179–14183.
- [18] J. Yang, W. Li, D. Wang, Y. Li, *Adv. Mater.* 32 (2020) 2003300.
- [19] F.D. Speck, F.S.M. Ali, M.T.Y. Paul, R.K. Singh, T. Böhm, A. Hofer, O. Kasian, S. Thiele, J. Bachmann, D.R. Dekel, T. Kallio, S. Cherevko, *Chem. Mater.* 32 (2020) 7716–7724.
- [20] F. Zou, Y.-M. Chen, K. Liu, Z. Yu, W. Liang, S.M. Bhaway, M. Gao, Y. Zhu, *ACS Nano* 10 (2016) 377–386.
- [21] L. Yan, Y. Xu, P. Chen, S. Zhang, H. Jiang, L. Yang, Y. Wang, L. Zhang, J. Shen, X. Zhao, L. Wang, *Adv. Mater.* 32 (2020) 2003313.
- [22] L. Yan, H. Jiang, Y. Wang, L. Li, X. Gu, P. Dai, D. Liu, S.-F. Tang, G. Zhao, X. Zhao, K.M. Thomas, *Electrochim. Acta* 297 (2019) 755–766.
- [23] A. Tang, C. Wan, X. Hu, X. Ju, *Nano Res.* 14 (2021) 4063–4072.
- [24] G. Kresse, J. Furthmüller, *Comput. Mater. Sci.* 6 (1996) 15–50.
- [25] G. Kresse, J. Furthmüller, *Phys. Rev. B* 54 (1996) 11169–11186.
- [26] J.P. Perdew, K. Burke, M. Ernzerhof, *Phys. Rev. Lett.* 77 (1996) 3865–3868.
- [27] P.E. Blöchl, *Phys. Rev. B* 50 (1994) 17953–17979.
- [28] S. Zhang, H. Xue, W.-L. Li, J. Sun, N. Guo, T. Song, H. Dong, J. Zhang, X. Ge, W. Zhang, *Q. Wang, Small* 17 (2021) 2102125.
- [29] A. Sunny, K. Balasubramanian, *J. Raman Spectrosc.* 52 (2021) 833–842.
- [30] Z. Li, L. Leng, S. Ji, M. Zhang, H. Liu, J. Gao, J. Zhang, J.H. Horton, Q. Xu, J. Zhu, *J. Energy Chem.* (2022), <https://doi.org/10.1016/j.jechem.2022.05.009>.
- [31] Y.-C. Yin, R.-X. Deng, D.-R. Yang, Y.-B. Sun, Z.-Q. Li, X.-H. Xia, *J. Phys. Chem. Lett.* 13 (2022) 4350–4356.
- [32] A. Sunny, K. Balasubramanian, *J. Phys. Chem. C* 124 (2020) 12636–12644.
- [33] N. Mironova-Ulmane, A. Kuzmin, I. Steins, J. Grabis, I. Sildos, M. Pārs, *J. Phys. Conf. Ser.* 93 (2007) 012039.
- [34] G. Liu, J. Li, J. Fu, G. Jiang, G. Lui, D. Luo, Y.P. Deng, J. Zhang, Z.P. Cano, A. Yu, D. Su, Z. Bai, L. Yang, Z. Chen, *Adv. Mater.* 31 (2019) 1806761.
- [35] H. Xue, A. Meng, T. Yang, Z. Li, C. Chen, *J. Energy Chem.* 71 (2022) 639–651.
- [36] Y. Cao, Y. Su, L. Xu, X. Yang, Z. Han, R. Cao, G. Li, *J. Energy Chem.* 71 (2022) 167–173.
- [37] L. Gong, H. Zhang, Y. Wang, E. Luo, K. Li, L. Gao, Y. Wang, Z. Wu, Z. Jin, J. Ge, Z. Jiang, C. Liu, W. Xing, *Angew. Chem. Int. Ed.* 59 (2020) 13923–13928.
- [38] S. Dou, C. Hu, L. Shi, W. Zhang, S. Zhou, P. Yan, L. D'Souza, T.T. Isimjan, X. Yang, *ChemCatChem* 13 (2021) 3628–3635.
- [39] Z. Liu, X. Yang, G. Hu, L. Feng, *ACS Sustain. Chem. Eng.* 8 (2020) 9136–9144.
- [40] Y. Yao, Y. Zhu, C. Pan, C. Wang, S. Hu, W. Xiao, X. Chi, Y. Fang, J. Yang, H. Deng, S. Xiao, J. Li, Z. Luo, Y. Guo, *J. Am. Chem. Soc.* 143 (2021) 8720–8730.
- [41] Z. Wei, Z. Zhao, J. Wang, Q. Zhou, C. Zhao, Z. Yao, J. Wang, *J. Mater. Chem. A* 9 (2021) 10160–10168.
- [42] Q. Peng, Q. He, Y. Hu, T.T. Isimjan, R. Hou, X. Yang, *J. Energy Chem.* 65 (2022) 574–582.
- [43] Y. Huang, Q. Gong, X. Song, K. Feng, K. Nie, F. Zhao, Y. Wang, M. Zeng, J. Zhong, Y. Li, *ACS Nano* 10 (2016) 11337–11343.

- [44] T.Y. Yoo, J.M. Yoo, A.K. Sinha, M.S. Bootharaju, E. Jung, H.S. Lee, B.-H. Lee, J. Kim, W.H. Antink, Y.M. Kim, J. Lee, E. Lee, D.W. Lee, S.-P. Cho, S.J. Yoo, Y.-E. Sung, T. Hyeon, *J. Am. Chem. Soc.* 142 (2020) 14190–14200.
- [45] Y. Feng, K. Song, W. Zhang, X. Zhou, S.J. Yoo, J.-G. Kim, S. Qiao, Y. Qi, X. Zou, Z. Chen, T. Qin, N. Yue, Z. Wang, D. Li, W. Zheng, *J. Energy Chem.* 70 (2022) 211–218.
- [46] Z. Zhou, Y. Liu, J. Zhang, H. Pang, G. Zhu, *Electrochem. Commun.* 121 (2020) 106871.
- [47] W. Sheng, Z. Zhuang, M. Gao, J. Zheng, J.G. Chen, Y. Yan, *Nat. Commun.* 6 (2015) 5848.
- [48] J. Wu, Y. Zhou, H. Nie, K. Wei, H. Huang, F. Liao, Y. Liu, M. Shao, Z. Kang, *J. Energy Chem.* 66 (2022) 61–67.
- [49] J. Zhang, X. Qu, L. Shen, G. Li, T. Zhang, J. Zheng, L. Ji, W. Yan, Y. Han, X. Cheng, Y. Jiang, S. Sun, *Small* 17 (2021) 2006698.
- [50] J. Cai, X. Liao, P. Li, Q. Wang, H. Huang, Z. Lyu, J. Lin, S. Xie, *Chem. Eng. J.* 429 (2022) 132414.
- [51] D. Liu, S. Lu, Y. Xue, Z. Guan, J. Fang, W. Zhu, Z. Zhuang, *Nano Energy* 59 (2019) 26–32.
- [52] X. Ji, Y. Lin, J. Zeng, Z. Ren, Z. Lin, Y. Mu, Y. Qiu, J. Yu, *Nat. Commun.* 12 (2021) 1380.
- [53] B. Zhang, G. Zhao, B. Zhang, L. Xia, Y. Jiang, T. Ma, M. Gao, W. Sun, H. Pan, *Adv. Mater.* 33 (2021) 2105400.
- [54] D. Strmcnik, M. Uchimura, C. Wang, R. Subbaraman, N. Danilovic, D. van der Vliet, A.P. Paulikas, V.R. Stamenkovic, N.M. Markovic, *Nat. Chem.* 5 (2013) 300–306.
- [55] B. Qjin, H. Yu, X. Gao, D. Yao, X. Sun, W. Song, B. Yi, Z. Shao, *J. Mater. Chem. A* 6 (2018) 20374–20382.
- [56] Z. Gao, G. Fan, M. Liu, L. Yang, F. Li, *Appl. Catal. B: Environ.* 237 (2018) 649–659.
- [57] M. Guo, M. Xu, Y. Qu, C. Hu, P. Yan, T.T. Isimjan, X. Yang, *Appl. Catal. B: Environ.* 297 (2021) 120415.
- [58] T. Zhang, M.-Y. Wu, D.-Y. Yan, J. Mao, H. Liu, W.-B. Hu, X.-W. Du, T. Ling, S.-Z. Qiao, *Nano Energy* 43 (2018) 103–109.